

## Both genome and cytosol dynamics change in *E. coli* challenged with sublethal rifampicin

This content has been downloaded from IOPscience. Please scroll down to see the full text.

2017 Phys. Biol. 14 015005

(<http://iopscience.iop.org/1478-3975/14/1/015005>)

View [the table of contents for this issue](#), or go to the [journal homepage](#) for more

### Download details:

This content was downloaded by: pc245

IP Address: 131.111.75.157

This content was downloaded on 16/05/2017 at 12:19

Please note that [terms and conditions apply](#).

You may also be interested in:

[Physical descriptions of the bacterial nucleoid at large scales, and their biological implications](#)

Vincenzo G Benza, Bruno Bassetti, Kevin D Dorfman et al.

[Compaction of bacterial genomic DNA: clarifying the concepts](#)

Marc Joyeux

[Comparison of the theoretical and real-world evolutionary potential of a genetic circuit](#)

M Razo-Mejia, J Q Boedicker, D Jones et al.

[Correlative super-resolution imaging of RNA polymerase distribution and dynamics, bacterial membrane and chromosomal structure in Escherichia coli](#)

Christoph Spahn, Francesca Cella-Zannacchi, Ulrike Endesfelder et al.

[Transcription closed and open complex dynamics studies reveal balance between genetic determinants and co-factors](#)

Adrien Sala, Muhammad Shoaib, Olga Anufrieva et al.

[Robustness of the division symmetry in Escherichia coli and functional consequences of symmetry breaking](#)

Abhishekh Gupta, Jason Lloyd-Price, Samuel M D Oliveira et al.

[Noisy cell growth rate leads to fluctuating protein concentration in bacteria](#)

Saburo Tsuru, Junya Ichinose, Akiko Kashiwagi et al.

[Anomalous transport in the crowded world of biological cells](#)

Felix Höfling and Thomas Franosch

## Physical Biology

## OPEN ACCESS



## PAPER

Both genome and cytosol dynamics change in *E. coli* challenged with sublethal rifampicin

## RECEIVED

11 October 2016

## REVISED

18 January 2017

## ACCEPTED FOR PUBLICATION

23 January 2017

## PUBLISHED

16 February 2017

Original content from this work may be used under the terms of the [Creative Commons Attribution 3.0 licence](https://creativecommons.org/licenses/by/3.0/).

Any further distribution of this work must maintain attribution to the author(s) and the title of the work, journal citation and DOI.

Michal Wlodarski<sup>1</sup>, Bianca Raciti<sup>1</sup>, Jurij Kotar<sup>1</sup>, Marco Cosentino Lagomarsino<sup>2</sup>, Gillian M Fraser<sup>3</sup> and Pietro Cicuta<sup>1</sup><sup>1</sup> Biological and Soft Systems, Cavendish Laboratory, University of Cambridge, United Kingdom<sup>2</sup> Laboratory of Computational and Quantitative Biology (UMR 7238 CNRS), Université Pierre et Marie Curie, Paris, France<sup>3</sup> Department of Pathology, University of Cambridge, United KingdomE-mail: [pc245@cam.ac.uk](mailto:pc245@cam.ac.uk)**Keywords:** bacteria chromosome, sublethal antibiotic, nucleoid dynamicsSupplementary material for this article is available [online](#)**Abstract**

While the action of many antimicrobial drugs is well understood at the molecular level, a systems-level physiological response to antibiotics remains largely unexplored. This work considers fluctuation dynamics of both the chromosome and cytosol in *Escherichia coli*, and their response to sublethal treatments of a clinically important antibiotic, rifampicin. We precisely quantify the changes in dynamics of chromosomal loci and cytosolic aggregates (a rheovirus nonstructural protein known as  $\mu$ NS-GFP), measuring short time-scale displacements across several hours of drug exposure. To achieve this we develop an empirical method correcting for photo-bleaching and loci size effects. This procedure allows us to characterize the dynamic response to rifampicin in different growth conditions, including a customised microfluidic device. We find that sub-lethal doses of rifampicin cause a small but consistent increase in motility of both the chromosomal loci and cytosolic aggregates. Chromosomal and cytosolic responses are consistent with each other and between different growth conditions.

**1. Introduction**

For over 70 years antibiotics have been used to control bacterial infections and have become an essential component of modern health care [1]. Simultaneously, with the rapidly growing incidence of antibiotic resistance [2] and relatively low antibiotic discovery rates [3], lack of adequate treatment options was recognised as a serious concern of a global and urgent significance [4, 5]. Consequently, a fundamental understanding of bacterial behaviour, and bacterial responses to treatments in particular, is one of the key objectives of modern medical research. Currently, many important aspects of how antibiotics affect bacterial physiology remain unknown. Although attempts have been made to provide a more holistic picture of antibiotic effects (e.g. through DNA microarray studies on global gene expression [6]), systems-level physiological responses such as effects on gene regulatory networks and on the macromolecular composition of cells (e.g. the concentration of ribosomes, protein-DNA ratio) remain largely unexplored.

Bacterial DNA is several orders of magnitude longer than the cell length and therefore it must be organised and packaged with associated proteins and RNA into a compact structure called the nucleoid [7, 8]. The strong compaction of nucleoid arises from a combination of forces generated by cellular confinement, macromolecular crowders, nucleoid-associated proteins (NAPs), and DNA supercoiling [9, 10]. While highly condensed, the physical organisation of the nucleoid must allow for protein diffusion, gene expression [9, 11], as well as efficient DNA replication and segregation [12]. Numerous factors such as signalling (e.g. cGMP) and alarmone (e.g. ppGpp) [13] molecules as well as NAPs (e.g. Fis, H-NS, IHF, HU, Dps, MatP) [8, 14] play a role in modulating the local DNA topology ensuring sufficient energy (negative supercoiling) is available to enable transcription. In this picture, local physical properties of a bacterial chromosomal locus reflect its nucleo-protein environment and can directly influence its biological activity.

High-frequency dynamics (fluctuations) of chromosomal loci can be followed with high time-resolution

microscopy [15–17]. At time-scales over a minute, chromosomal movement is dominated by segregation, showing up as directed (ballistic) motion [15, 18]. However, on time-scales much shorter than this, displacements are interpreted as fluctuations in a complex environment; in physical systems this is commonly referred to as ‘micro-rheology’ [19, 20]. The properties of a medium are measured by tracking and quantifying the mean square displacement (MSD) of a tracer travelling through the medium.

The MSD is defined as:

$$\text{MSD}(\tau) = \langle (\mathbf{x}(t + \tau) - \mathbf{x}(t))^2 \rangle, \quad (1)$$

where  $\mathbf{x}$  is the position of a particle at a given time,  $t$  is the initial time of observation, and  $\tau$  is the observation time scale (lag time) [21]. The average in equation (1) can be either a ‘time average’ of the initial times  $t$  for a single locus track, or an ‘ensemble average’ of multiple tracks at the fixed initial time  $t$ , or both, as used in this work. In complex viscoelastic fluids, such as the bacterial nucleoid and cytosol, random motion is subdiffusive, with the MSD scaling as  $\tau^\alpha$  with the exponent  $0 < \alpha < 1$  (for diffusion,  $\alpha = 1$ ) [16] with the amplitude proportional to driving forces and inversely proportional to the viscoelastic resistance of the surrounding medium [22].

By measuring MSD of chromosomal loci at short (<100 s) time-scales, Weber *et al* [16] revealed that the ‘jiggling’ motion of chromosomal loci is subdiffusive with the power law exponent  $\alpha \simeq 0.4$ , as well as superthermal, meaning it is characterised by much stronger temperature dependence than predicted by the Stokes–Einstein relation [22, 24]. The latter suggested a significant contribution from active (ATP-dependent) processes resulting in motion by active diffusion, potentially capable of speeding up diffusion-limited reactions [24]. Supporting these observations, Javer *et al* [25] reported that a small fraction (typically 2–5%) of tracked chromosomal loci display super-diffusive dynamics and seemingly directed, near-ballistic trajectories again pointing to the presence of non-trivial active or stress-release contributions to chromosomal motion. The amplitude of this motion varies as a function of the chromosomal coordinate, with regions located closer to the origin of replication (Ori macrodomain) showing MSD up to 4-fold larger compared to regions near the terminus of replication (Ter macrodomain) [17]. The latter is likely due to MatP-mediated condensation [14] and possible tethering of the Ter region at certain stages of the cell cycle [26]. Previous work suggested an Ori–Ter gradient in supercoiling, which corresponds to the uneven distribution of DNA gyrase and HU sites [27] and is likely to also contribute to these differences. Functionally, varying local dynamics of the genetic loci can potentially contribute to differential expression of groups of genes as indicated by higher expression of genes (during the exponential phase of growth) belonging to the Ori-proximal region compared to the more distal regions.

Tracer objects in the cytosol also display subdiffusive motions, with non-trivial size dependence [28]. It is thus an open question whether one or other of the chromosome or the crowded cytosol (or both jointly) is causing the complex dynamics observed in the other. Consequently, in order to fully characterise genome dynamics, it is necessary to measure both motions. In a recent study, genetically encoded size-calibrated  $\mu\text{NS-GFP}$  cytosolic aggregates foreign to *E. coli* showed, similarly to chromosomal loci, metabolism-dependent motion. The size of cytosolic aggregates accentuated the effects of metabolism, with the difference in the MSD between metabolically active and inactive cells increasing with aggregate size [28].

Here, we first introduce a data treatment procedure for quantifying local fluctuations compensating for photo-bleaching as well as marker size effects. We then apply the procedure to study long-term (several hours) effects of sublethal rifampicin treatments on the short time-scale dynamics of *E. coli* chromosomal loci Ori2 (proximal to the replication origin) and Ter3 (proximal to the replication terminus) and cytosolic  $\mu\text{NS-GFP}$  aggregates in different growth conditions, including standard agar microcolonies and a customised microfluidic device. We find that sub-lethal doses of rifampicin cause a small but consistent increase in motility of both the chromosomal loci and cytosolic aggregates. In addition, chromosomal and cytosolic effects correlate throughout most of the treatment time.

## 2. Results

### 2.1. Empirical correction of marker photo-bleaching effects and MSD-size dependence.

We performed high-throughput tracking of chromosomal Ori2 and Ter3 loci and rheovirus nonstructural protein cytosolic  $\mu\text{NS-GFP}$  aggregates collecting in total about 67 000 tracks from up to 9 biological replicates per treatment condition (for details see table S1, supplementary materials ([stacks.iop.org/PhysBio/14/015005/mmedia](http://stacks.iop.org/PhysBio/14/015005/mmedia))), growing bacteria in standard agarose microcolonies (figure 1(A)) or in a customised microfluidic chip (figure 1(B)). Chromosomal Ori2 and Ter3 loci (figure 1(C)) consist of ParB–GFP molecules polymerised at *parS* sites in Ori and Ter chromosomal macrodomains (MD), respectively. These loci were previously found to show large (up to 4-fold) differences in MSD [17]. Cytosolic  $\mu\text{NS-GFP}$  aggregates consist of GFP-labelled proteins of a rheovirus origin foreign to *E. coli* bacteria and capable of self-assembly into trackable particles of variable size (figure 1(D)) [28]. The MSD versus lag time curves of the three markers are compatible with a power law with exponent  $\alpha$ , with chromosomal loci exploring space slower ( $\alpha \simeq 0.4$ ) than the cytosolic aggregates ( $\alpha \simeq 0.6$ ) (figure 1(E)).

Our markers show wide intensity (size) distributions (100–4000 AU) and large coefficients of variation (0.87–0.92, depending on the marker), with

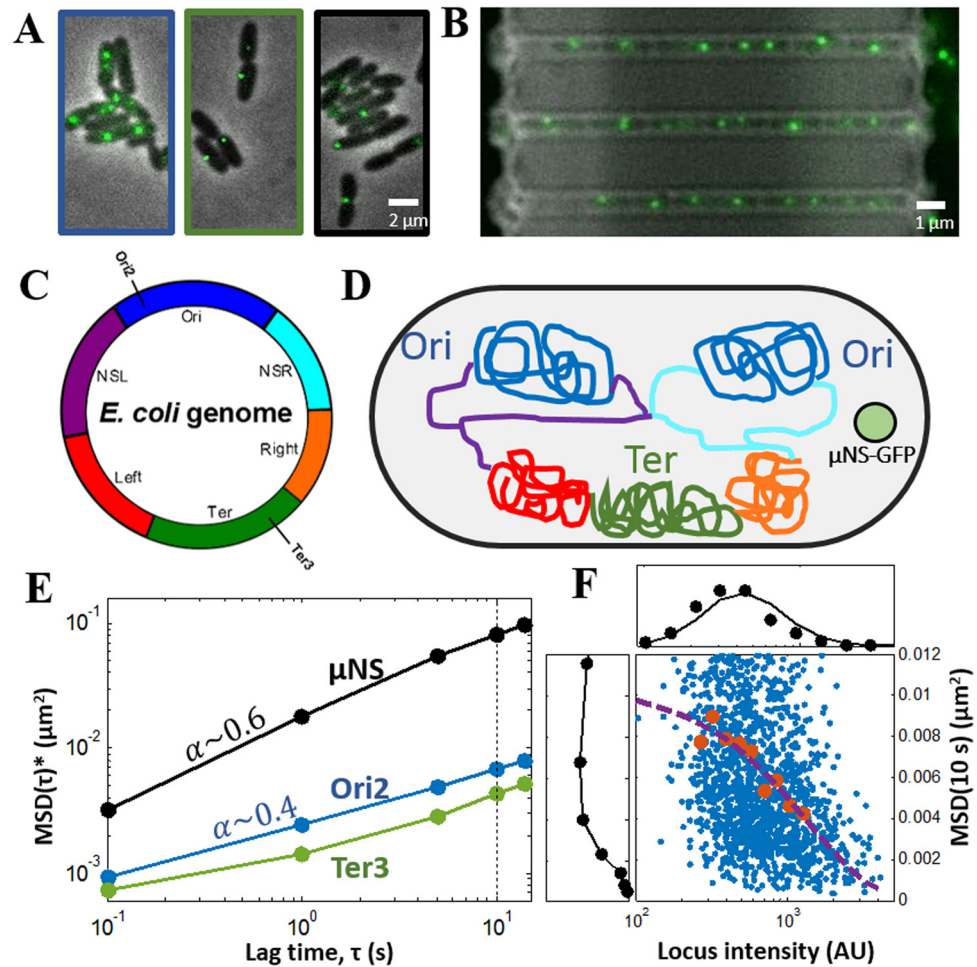


**Figure 1.** Illustration of the experiment and basic results. (A) Example phase-contrast images of agarose microcolonies of the three strains, with fluorescent markers (left, Ori2; middle, Ter3; right,  $\mu$ NS) overlaid in green. (B) Example bright-field image of three microchannels loaded with *E. coli* bacteria with Ori2 loci overlaid in green. (C) Schematic representation of the *E. coli* genome with colour-coded four macrodomains (MD; Ori, origin of replication; Right; Ter, terminus of replication; and Left MD) and two non-structured regions (NSL, left non-structured region; NSR, right non-structured region), and indicated Ori2 and Ter3 loci relative positions [23]. (D) Schematic not-to-scale representation of a dividing *E. coli* chromosome and a cytosolic  $\mu$ NS-GFP aggregate (green). Ori MD replicates and segregates first, followed by non-structured regions and then Left and Right MDs, and finishing with Ter MD. The cytosolic  $\mu$ NS-GFP aggregate (foreign to *E. coli*) assembles and suspends in the cytoplasm. (E) MSD as a function of a lag time ( $\tau$ ) for the three fluorescent markers tracked in this work. Marker photo-bleaching and size effects are corrected with the data treatment procedure as indicated by a star sign (\*). The 10 s lag time selected for analysis is indicated with a dashed line.  $\text{MSD}(\tau)^*$  scales as  $\tau^\alpha$  with chromosomal loci exploring space slower ( $\alpha \approx 0.4$ ) than the cytosolic aggregates ( $\alpha \approx 0.6$ ). (F) 'Raw' data MSD(10 s) versus locus intensity, from an example Ori2 loci data set, illustrating the wide MSD (left, part of the distribution tail not shown) and intensity (top) distributions as well as MSD-intensity (size) dependence (dashed violet line; function fitting as in figure 3). Bigger (brighter) loci generally show lower motility compared to smaller (fainter) ones.

fainter (having fewer GFP molecules) markers generally having higher MSD compared to brighter ones (having more GFP molecules) (figure 1(F)). In addition, markers photo-bleach when illuminated during image acquisition. This is important in the experiments reported here because the same fields of view are imaged repeatedly over time. In order to precisely quantify the magnitude of changes to marker dynamics, we accounted for photo-bleaching effects, as well as for dependence of MSD on the size of the fluorescent markers.

Chromosomal loci photo-bleach to a finite baseline value due to a continuous production of ParB-GFP molecules (figure 2) while cytosolic aggregates decay to zero (figure S1 in supplementary materials), as IPTG-induced  $\mu$ NS-GFP production is stopped by

washing the cells directly before experiments. In order to measure the photo-bleaching rate, we consider frequency distributions of recorded loci intensities for individual measurement time points (figure 2(A); figure S2 and equation (S1) in supplementary materials). The decay in the distributions means (dashed vertical lines in figure 2(A) and black solid circles in figure 2(B)) represents a population photo-bleaching profile that can be fitted (figure 2(B), blue line) with an exponential function,

$$I_t = I_0 e^{-\lambda(t-t_0)} + B, \quad (2)$$

where  $I_t$  is initial locus intensity at time  $t$ ,  $I_0$  is initial locus intensity at time  $t_0$ ,  $t_0$  is the initial measurement time (fixed at 20 min for all experiments), and  $\lambda$  and  $B$  are free fitting parameters and represent the

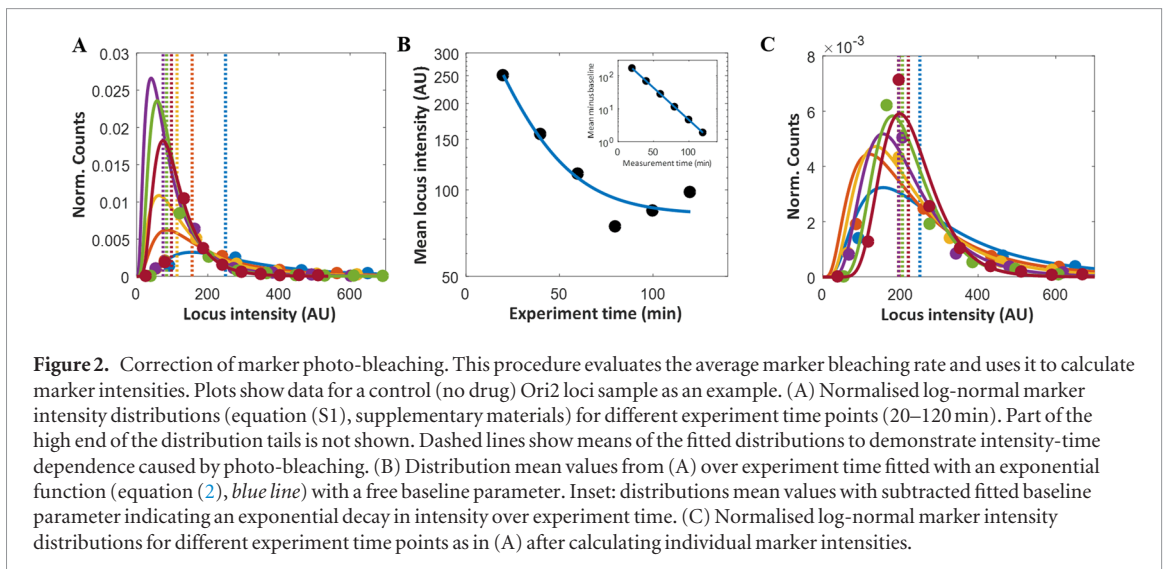


photo-bleaching rate and the intensity baseline respectively (this is valid for chromosomal loci only, see equation (S2) in supplementary materials for  $\mu$ NS-GFP). Initial intensity is defined as the mean locus intensity as recorded in the first 10 frames of a movie. For each tracked marker, we use its population photo-bleaching rate,  $\lambda$ , to evaluate, using equation (2), its original intensity (pre-photo-bleaching,  $I_0$ ) assuming an exponential decay in intensity.

The pre-photo-bleaching intensity of each locus at each measurement time point is used to correct for marker MSD-size dependence (figure 3). This procedure uses a control (no drug) Ori2 dataset generated previously by Javer *et al* [17] consisting of about 2000 tracks collected using the same experimental set-up and analysis methods. The procedure defines 20 logarithmically-spaced bins along a 100–4000 AU locus intensity range and evaluates median MSD for each bin. Medians for bins where the number of loci is equal or greater than the mean number of loci per bin (red solid circles in figure 3(A)) are fitted with an exponential function (figure 3(A), dashed violet line; equation (S3) in supplementary materials) that we then use to normalise our data. To flatten this normalisation curve, we select the statistically strongest ‘reference’ intensity bin and generate a 20-element correction factor vector that normalises the median MSD values of all other bins to that reference value (black solid circles in figure 3(B)). This approach minimises locus size effects while including contributions from all tracked loci. We repeat this for five lag times (0.1, 1.0, 5.0, 10, and 14 s; figure 3(C)) and use the correction vectors to normalise our data.

To appreciate the effects of the correction procedure on a control data set, compare panels A + C (before correction) and B + D (after correction) in figure 4. Before correction, there is a strong MSD-intensity (size) dependence (figure 4(A)) as well as a considerable change in median MSD and intensity over measurement time (figure 4(C)). Our procedure effectively eliminates photo-bleaching effects (top side plot distribution in figure 4(B)) and largely reduces MSD-size

dependence (generally flat fitted curves in figure 4(B)) as well as reveals only little change in MSD over measurement time (left side plot distribution in figure 4(B)). In addition, our procedure reveals a transient (40–100 min) decrease in MSD, consistent with fluctuations in growth rate of the control data sets (figure S3 in supplementary materials), possibly due to bacteria adapting to new growth conditions (figure 4(D)).

## 2.2. Rifampicin causes consistent increase in motility of both chromosomal loci and cytosolic aggregates

We use the data treatment procedure to study effects of rifampicin on short time-scale dynamics of chromosomal Ori2 and Ter3 loci and cytosolic  $\mu$ NS-GFP aggregates. Rifampicin is a transcription inhibitor commonly used in treatment of several types of bacterial infections. We use sub-lethal rifampicin concentrations determined for individual strains (for details see Materials and Methods). At these concentrations, effects on cell length and elongation rate are not significant and only small fluctuations are present (figure S3 in supplementary materials).

The control (no drug) data sets show highest motility for cytosolic aggregates ( $0.04$ – $0.08 \mu\text{m}^2$ , depending on growth conditions) while chromosomal loci show MSD an order of magnitude lower with Ori2 loci exploring space quicker than Ter3 loci ( $\approx 4.0 \times 10^{-3}$  and  $2.5 \times 10^{-3} \mu\text{m}^2$  on agar;  $\approx 6.0 \times 10^{-3}$  and  $4.0 \times 10^{-3} \mu\text{m}^2$  in chip, respectively), as expected. Agarose and chip data are less consistent for faster moving markers. Possibly due to relatively higher motilities of Ori2 loci and  $\mu$ NS-GFP aggregates, these markers show larger variability in motility when measured for different biological replicates. All agarose data sets show a transient decrease in motility after 40 min, possibly due to bacteria adapting to new growth conditions. In the microfluidic device, where we equilibrate bacteria for 6 h prior to exposure to rifampicin, we observe no such decrease.

Treatment with rifampicin causes a small increase in motility of all three markers (figure 5). Effects are con-

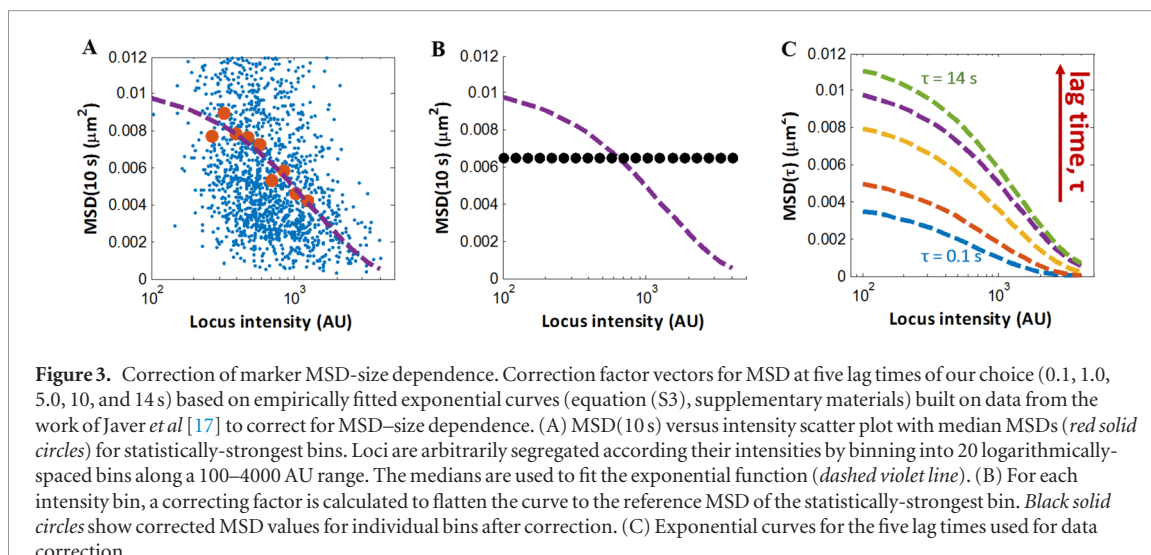


**Figure 3.** Correction of marker MSD-size dependence. Correction factor vectors for MSD at five lag times of our choice (0.1, 1.0, 5.0, 10, and 14 s) based on empirically fitted exponential curves (equation (S3), supplementary materials) built on data from the work of Javer *et al* [17] to correct for MSD-size dependence. (A) MSD(10 s) versus intensity scatter plot with median MSDs (red solid circles) for statistically-strongest bins. Loci are arbitrarily segregated according to their intensities by binning into 20 logarithmically-spaced bins along a 100–4000 AU range. The medians are used to fit the exponential function (dashed violet line). (B) For each intensity bin, a correcting factor is calculated to flatten the curve to the reference MSD of the statistically-strongest bin. Black solid circles show corrected MSD values for individual bins after correction. (C) Exponential curves for the five lag times used for data correction.

sistent throughout the drug treatment time (up to 2 h for agarose microcolonies and up to 6 h for microfluidic device) and between the two growth conditions. Error bars for agarose data sets (standard deviation of the median;  $n = 9$  and  $n = 6$  biological replicates for chromosomal and cytosolic markers, respectively) are shown in figure 6. On agarose, where rifampicin is present at  $t = 0$  min effects are already evident at the first measurement ( $t = 20$  min) except for Ori2 loci, where an increase in motility is seen only after 100 min. In chip, effects for all markers are already evident at the first measurement time (1 h).

To compare chromosomal responses directly, we considered relative changes (as treated-to-control (MSD(10 s)\* ratio) in motility of Ori2 and Ter3 loci for individual treatment times and for the two growth conditions (figure 7(A), solid and empty marker points for agarose and chip, respectively). Motility of Ter3 loci increases earlier compared to Ori2 loci and the fold change is larger (+0.1 and +0.06, respectively). Chip data is generally consistent, however, the fold change in Ter3 loci motility is half compared to change measured for agarose microcolonies. Analogously, we compare chromosomal and cytosolic responses directly (figure 7(B)), revealing that cytosolic aggregates show the fold change (+0.05) in motility comparable to Ori2 loci (+0.06) and that the directions of chromosomal and cytosolic responses are consistent throughout the treatment time, except for the final time point. Data from agarose pads and microfluidic channels are generally consistent.

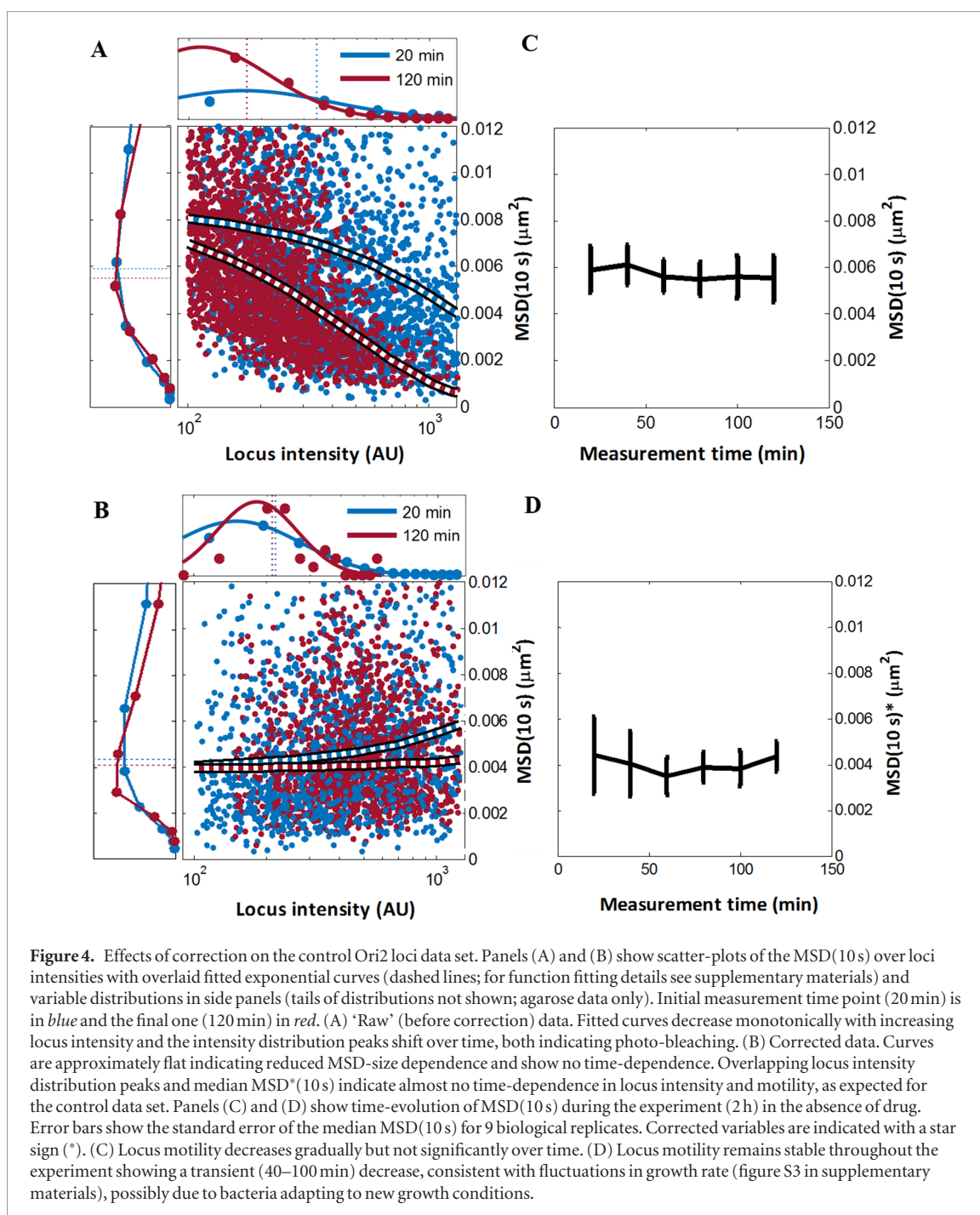
### 3. Discussion

The empirical approach to data treatment developed here accounts for both marker photo-bleaching and marker size effects, and enables precise quantification of the magnitude of changes to chromosomal and cytosolic marker dynamics. Accounting for photo-bleaching makes it possible to perform long-time (several hours) measurements, necessary to study

effects of antibiotics, which often exert measurable effects only after a prolonged exposure. The correction of marker MSD-size dependence, reduces bias arising from physical effects such as caging and metabolism-dependent contributions to motion, which were shown to depend on marker size [28]. Previous studies on short time-scale genome [15–17, 24, 25] and cytosol dynamics [28] were limited to single dynamics measurements and did not consider these significant corrections.

Current insight into how antibiotics affect genome and cytosol dynamics is limited. Weber *et al* studied effects of several antibiotics including rifampicin, which exerted nonmonotonic effects on chromosomal loci motility. After a 1 min treatment, motility decreased slightly but significantly and consistently. After longer treatments ( $\leq 30$  min), motility increased and plateaued at an approximately two-fold greater magnitude. To explain treatment time scale-dependent effects, the authors hypothesised that the initial decrease in loci motility was due to RNA polymerase (RNAP) inhibition during mRNA lifetime (mRNA  $t_{1/2} \approx 2$ –4 min [29]), while at longer ( $\geq 5$  min) times as the cellular pool of mRNA decayed, the effective viscosity of the cytoplasm decreased resulting in faster loci motion [24]. At the global level, Cabrera *et al* proposed that rifampicin causes nucleoid expansion as a direct result of RNAP foci dissociation [30]. Conversely, Bakshi *et al* suggested that the effects are RNAP-independent and that instead rifampicin-induced mRNA depletion causes polysome and ribosome dissociation into individual ribosomal subunits, which mix with and expand the nucleoid [31]. As we discuss now, nucleoid expansion potentially results in an increase in local chromosomal dynamics.

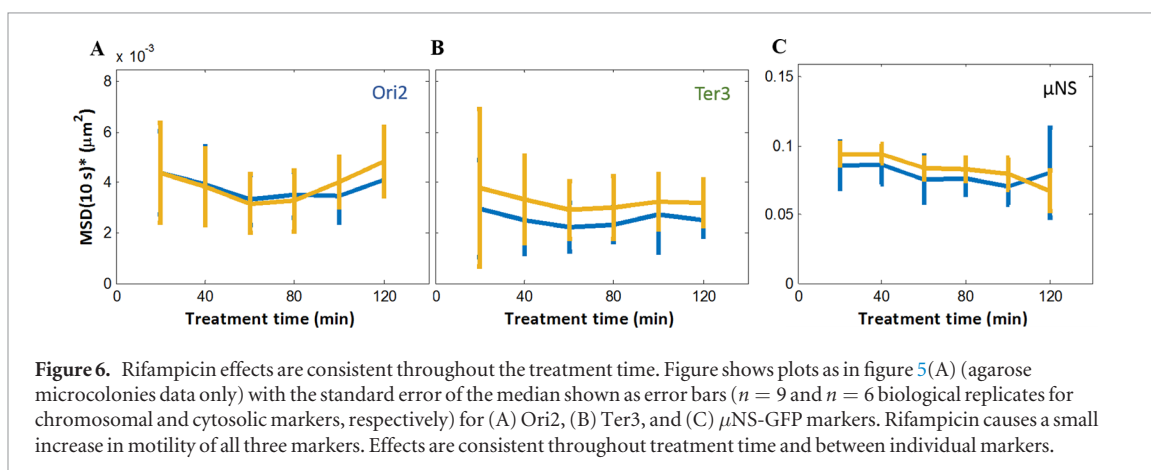
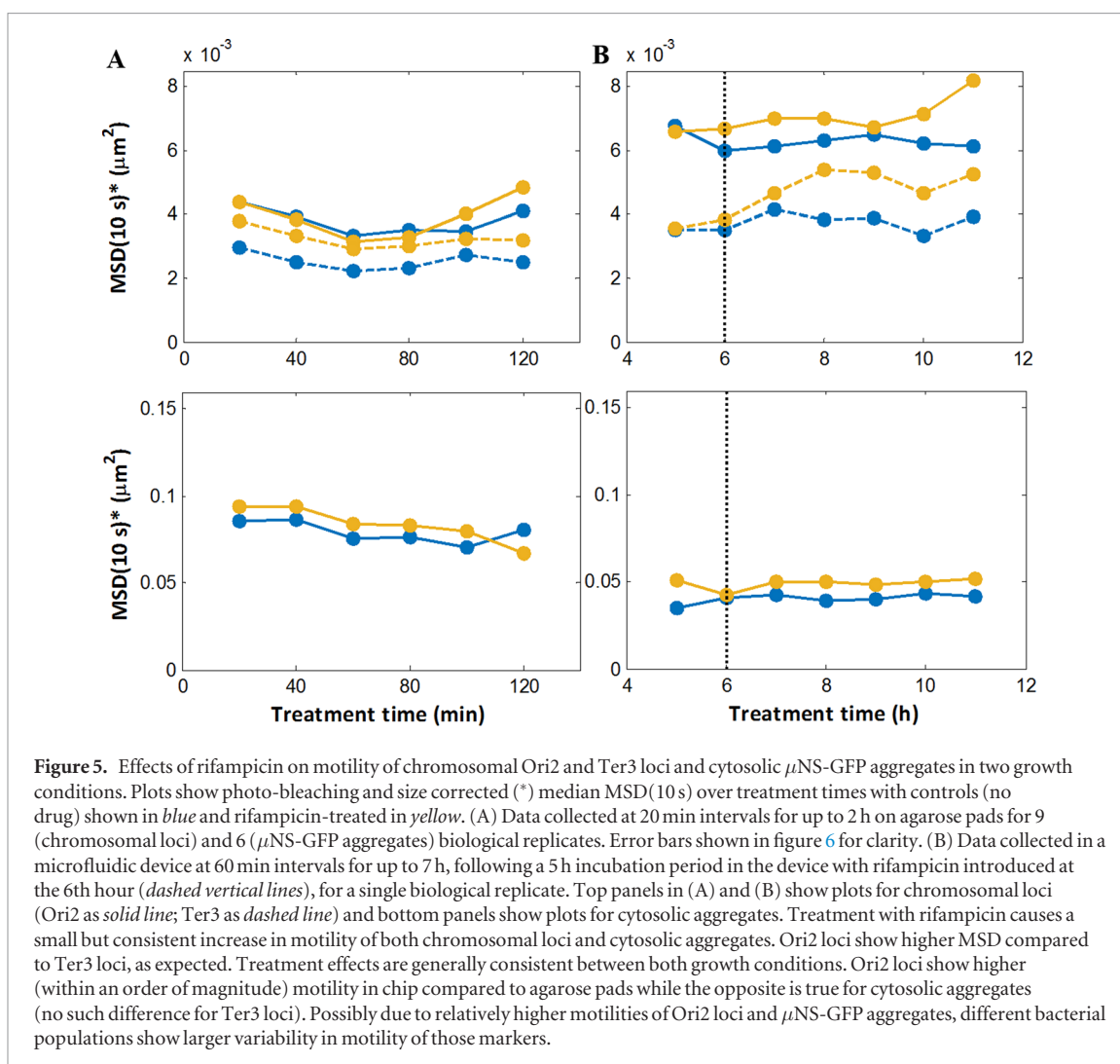
In general agreement with studies by Weber *et al* [24], Cabrera *et al* [30], and Bakshi *et al* [31], we show that sub-lethal treatment with rifampicin causes a small and consistent increase in short time-scale motility of Ori2 and Ter3 chromosomal loci. We also confirm higher motility of Ori2 loci compared to Ter3 loci as reported previously [17], and demonstrate that this



result is stable for hours for exponentially growing cells. We hypothesise that the amplitude of locus short-time scale motion is a measure of the level of its local physical compaction. Notably, we show that the initially more relaxed locus, Ori2, relaxed less when treated (fold change +0.06) if compared to the initially more compacted locus, Ter3 (fold change +0.1). We speculate this may suggest a functional limit to maximal relaxation of a genetic locus and the ability of a bacterial cell to alter gene physical environment flexibly depending on external stimuli and on gene position in the genome. Since sub-lethal rifampicin concentrations have little effect on growth rate, our work suggests the presence of broad off-target effects of clinically sub-optimal antibiotic doses, including possible effects on

intercellular communication as reported previously for bacterial communities [32].

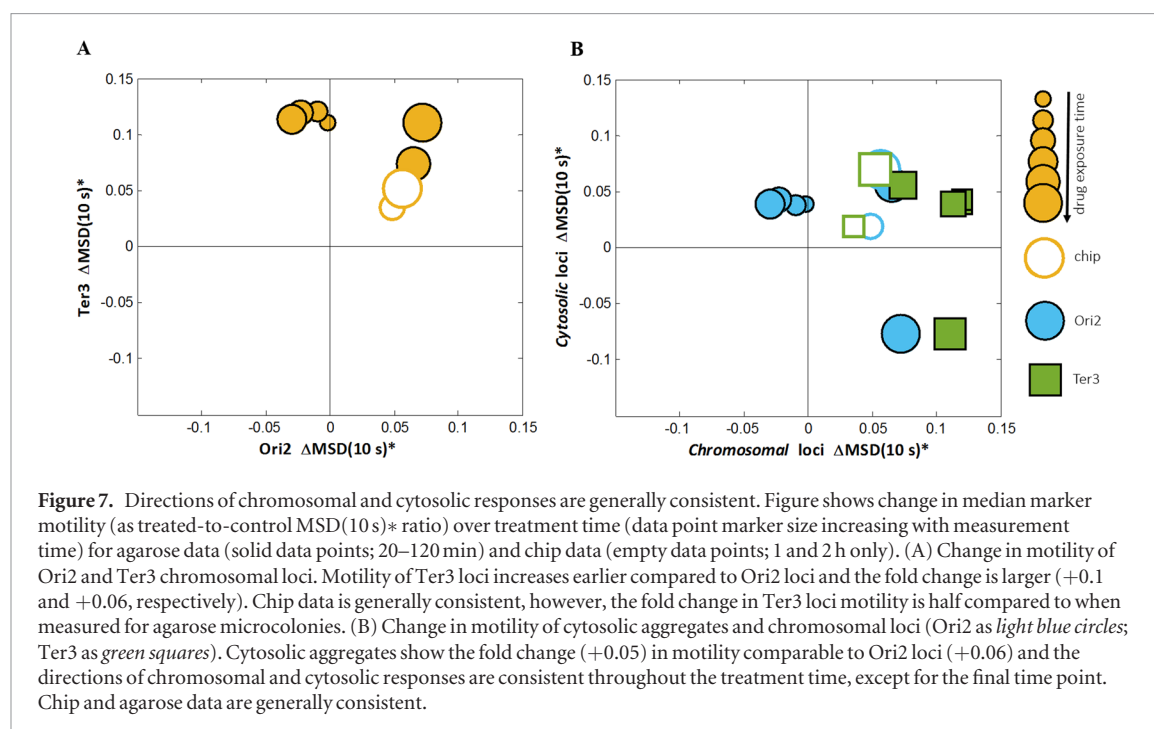
Interactions of crowded cytosol components affect chromosome energy states [9, 31], and so in order to fully characterise genome dynamics, we measured motions of both the chromosome and cytosol. To date only one study considered effects of antibiotics on the cytosol dynamics with relatively high doses used to switch off specific cellular processes and the MSD measured for long (minutes-hours) lag times [28]. We show that cytosolic aggregates in treated cells generally display a small but consistent increase (fold change +0.05) in short time scale motility comparable to that seen in treated Ori2 loci (fold change +0.06), and that directions of chromosomal and cytosolic responses are generally consistent throughout the treatment time.



Following Weber *et al* [24] and Bakshi *et al* [31], we speculate that RNAP inhibition and mRNA pool decay combined with subsequent ribosomal subunit-nucleoid mixing cause a decrease in cytosol viscosity and nucleoid expansion, ultimately increasing cytosolic aggregate and chromosomal loci motility.

One limitation of the data treatment procedure presented here is that corrections are computed from population-averages, and hence need a large sample of data. While extracting photo-bleaching profiles of individual markers is possible, it may be problematic, especially

for faster-moving markers such as cytosolic aggregates. Additionally, since a formal physical model describing size-dependent marker motion at short time-scales in live cells has not been developed yet, in the future, a physical model describing tracer size-dependent motions of chromosomal loci and cytosolic aggregates in live cells may further improve the data treatment procedure and highlight aspects of biological and physical significance. Since local DNA topology and energy states are key to gene function, the antibiotic-induced changes to chromosomal loci dynamics observed here may at



least in part explain global gene expression changes reported previously for many antibiotics [6, 33, 34]. Future work may correlate physiological effects such as the ones measured here with transcriptomics and single-cell level gene expression experiments reporting on gene activity as a function of locus dynamics. Such experiments may include microfluidic growth platforms (e.g. [35–37]) to enable long-term monitoring of responses to dynamically modulated concentrations of antibiotics and their combinations.

## 4. Materials and methods

### 4.1. Strains and culture conditions

To investigate chromosomal dynamics we used *E. coli* strains with the ParB-GFP/ *parS* fluorescent labelling system (provided by the Olivier Espéli and Frédéric Boccard's laboratories [38]), as in our previous work [17]. These MG1655 strains have P1 *parS* sites inserted at Ori2 and Ter3 positions on the chromosome (3928 826 and 1341 067 chromosomal coordinates, respectively). Loci are assigned names according to the MD they belong to. Expression of the ParB-GFP fusion protein is driven by the pALA2705 plasmid. The ParB protein used in this system has 30 amino acids truncated at the N-terminus region. The excitation peak of the GFP is at 488 nm. No isopropyl  $\beta$ -D-1-thiogalactopyranoside (IPTG) induction was required to produce the ParB-GFP levels necessary to visualise and track loci.

To investigate cytosolic dynamics we used the *E. coli* CJW4617 strain (provided by Christine Jacobs-Wagner's laboratory) of a MG1655 background capable of expressing  $\mu$ NS-GFP fusion protein. The avian reovirus protein  $\mu$ NS is a self-assembling protein [39] and its C-terminal fragment can form globular cytoplasmic particles, even when fused to GFP [40].  $\mu$ NS-GFP

synthesis is under the control of the chromosomal IPTG-inducible promoter lac. In this strain, the lacY (lactose/IPTG permease encoding) gene is deleted from the lac operon. Crucially,  $\mu$ NS-GFP aggregates are unlikely to make specific interactions with components of the bacterial cytoplasm, given the evolutionary divergence between bacteria and the avian reovirus. We induced the synthesis of the aggregates with 1 mM IPTG for 3.5–4 h, centrifuged the pre-culture at 4000 rpm for 10 min, and stopped induction by washing with the growth medium (details below) directly before experiments. Induction of GFP- $\mu$ NS synthesis usually resulted in a single fluorescent focus per cell.

All chemical reagents were obtained from Sigma-Aldrich unless otherwise stated. Strains were kept at  $-80^{\circ}\text{C}$  in lysogeny broth (LB) + 25% glycerol stocks and were streaked on LB plates (containing ampicillin  $100\ \mu\text{g ml}^{-1}$  and chloramphenicol  $25\ \mu\text{g ml}^{-1}$ ) before experiments. Strains were grown overnight in LB at  $37^{\circ}\text{C}$  with ampicillin  $100\ \mu\text{g ml}^{-1}$ . Each biological replicate constituted a separate overnight culture. Overnight cultures were diluted 200:1 into M9 minimal salts (BD) supplemented with complementary salts (CS;  $\text{MgSO}_4$  2 mM,  $\text{CaCl}_2$  100  $\mu\text{M}$ , tryptophan 4  $\mu\text{g ml}^{-1}$ , and thymidine 5  $\mu\text{g ml}^{-1}$ ), 0.4% glucose (Glu), and 0.5% casamino acids (CAA; BD). Doubling times were 65 min (Ori2 and Ter3 MG1655 strains) and 80 min (CJW4617). Pre-cultures were grown at  $30^{\circ}\text{C}$  to an  $\text{OD}_{600}$  of 0.2–0.3 and transferred either onto agarose pads or loaded into microfluidic device for image acquisition.

### 4.2. Sample preparation for microscopy experiments

Agarose pads contained 1.5% agarose dissolved in the M9 + CS + Glu + CAA medium and (if required) a fixed concentration of rifampicin. Pads were 8 mm

in diameter and 0.5 mm in thickness. 2.5  $\mu\text{l}$  of the pre-culture were deposited on a pad under aseptic conditions. The pad was then sealed between a cover slip and a glass slide with a stack of 3 frame seals (Fisher Scientific) to ensure access to excess of oxygen. Under the microscope, the sample was maintained at 30 °C during image acquisition for 2 h, waiting for 20 min before taking the first video. Doubling times on agarose pads were 45 (Ori2 MG1655), 50 (Ter3 MG1655), and 63 (CJW4617)  $\pm$  10 min, measured for individual cells (about 550 cells per strain).

The microfluidic device (Kevin Dorfman's laboratories) realised in polydimethylsiloxane (PDMS) consisted of two main channels supplying fresh medium to and removing waste from submicron-sized channels capable of immobilising bacteria while allowing for exponential growth. Device was plasma-cleaned and bonded to a previously sonicated (10 min in isopropanol and 10 min in acetone) and plasma-cleaned cover slip. Bonded device was passivated for at least 1 h with a 2 mg ml<sup>-1</sup> bovine serum albumin (BSA) solution at 30 °C, then manually loaded with the pre-culture to ensure suitable loading of bacteria (assessed visually under the microscope). The M9 + CS + Glu + CAA medium containing 0.1 mg ml<sup>-1</sup> BSA was supplied at 4  $\mu\text{l min}^{-1}$  using an automated syringe pump (KD Scientific) throughout the experiment. Bacteria were allowed to equilibrate and populate channels for 6 h prior to a media switch (if required) to introduce rifampicin. The first video was taken 5 h after loading (1 h before the switch).

#### 4.3. Rifampicin concentrations

For agarose experiments, MIC of rifampicin was determined for each strain using a standard agar dilution MIC determination method [41]. MIC was 1.2–1.4  $\mu\text{g ml}^{-1}$  for all strains. Nominal sublethal concentration 1.0  $\mu\text{g ml}^{-1}$  was used for experiments. As agarose pads can absorb liquid, it is possible that dissolved rifampicin was diluted after loading the pad with pre-culture. Volume of an agarose pad was about 25  $\mu\text{l}$  and loaded pre-culture volume was 2.5  $\mu\text{l}$  resulting in an up to 1.1X dilution. However, smaller dilution is likely as some of the loaded pre-culture evaporated rather than was absorbed into the pad.

Working concentrations were determined separately for microfluidic experiments. Dose-response curves were constructed using a FLUOstar OMEGA 96-well plate reader (BMG Labtech) growing bacteria at 30 °C after diluting overnight cultures 200:1 into 300  $\mu\text{l}$  of M9 + CS + Glu + CAA medium containing a range of rifampicin concentrations, and measuring the OD<sub>600</sub> every 30 min for 12 h with shaking at 200 rpm (data not shown). Final OD<sub>600</sub> values were plotted as a function of rifampicin concentration and IC<sub>50</sub> (50% growth inhibition) concentrations of 2.7 (Ori2 MG1655), 3.7 (Ter3 MG1655), 2.9 (CJW4617)  $\mu\text{g ml}^{-1}$  were selected for experiments.

#### 4.4. Image acquisition

We used a Nikon Eclipse Ti-E inverted microscope with a Plan Apo VC 60X oil immersion objective (NA 1.40). Images were further magnified with a 2.5X TV adapter before detection on an Andor iXon X3 897 EM-CCD camera, capable of detecting single fluorophores and yielding a high signal-to-noise ratio to enable high marker localisation precision. During a typical experiment, at least 21 manually selected fields of view were scanned, each field of view containing about 30 fluorescent markers. Field of view scanning and image acquisition were automated using custom-written software. Focus was maintained during scanning with the Nikon perfect focus (PFS) hardware autofocus system. 45 s movies were acquired at a 9.6 frame-per-second frame rate with an exposure time of 102 ms, resulting in 441-frame long movies. At agarose pad experiments each field of view was scanned 6 times, 20 min apart (total experiment time 2 h), while at microfluidic experiments each field of view was scanned 7 times, 1 h apart (total experiment time 7 h).

#### 4.5. Image and data processing and analysis

Image analysis methods and data processing and analysis protocols including image feature extraction, marker trajectory linking, and MSD fitting algorithms were identical to those previously reported by Javer *et al* [17].

### Acknowledgments

We are very grateful to B Sclavi, E Brendon, M Panlilio, S Takamori, T Bertoni, and L Feriani for useful discussions. We thank F Boccard, O Espéli, C Jacobs–Wagner, and C Lesser for the gifts of bacterial strains. We also thank A Javer for analysis programs, K Dorfman and J Sheats for microfluidic device wafers, and E Nugent for help with microfluidics experiments. M W was supported by BBSRC Doctoral Training Programme, and B R, M C L and P C were supported by HFSP grants.

### References

- [1] Levy S B 1998 The challenge of antibiotic resistance *Sci. Am.* **278** 46–53
- [2] Penn C, Silva da Pessoa C, Rogers P and Struwe J 2014 Antimicrobial resistance: global report on surveillance *Technical Report* WHO
- [3] Butler M S, Blaskovich M and Cooper M 2013 Antibiotics in the clinical pipeline *J. Antibiot.* **66** 571–91
- [4] Laxminarayan R *et al* 2013 Antibiotic resistance—the need for global solutions *Lancet Infect. Dis.* **13** 1057–98
- [5] Livermore D M 2005 Minimising antibiotic resistance *Lancet Infect. Dis.* **5** 450–9
- [6] Lin J T, Connelly M B, Amolo C, Yaver D S and Otani S 2005 Global transcriptional response of *Bacillus subtilis* to treatment with subinhibitory concentrations of antibiotics that inhibit protein synthesis *Antimicrob. Agents Chemother.* **49** 1915–26
- [7] Stavans J and Oppenheim A 2006 DNA-protein interactions and bacterial chromosome architecture *Phys. Biol.* **3** R1–10

- [8] Dame R T 2005 The role of nucleoid-associated proteins in the organization and compaction of bacterial chromatin *Mol. Microbiol.* **56** 858–70
- [9] Benza V G, Bassetti B, Dorfman K D, Scolari V F, Cicuta P and Lagomarsino M C 2012 Physical descriptions of the bacterial nucleoid at large scales, and their biological implications *Rep. Prog. Phys.* **75** 076602
- [10] Travers A and Muskhelishvili G 2005 DNA supercoiling—a global transcriptional regulator for enterobacterial growth? *Nat. Rev. Microbiol.* **3** 157–69
- [11] Dorman C J 2013 Genome architecture and global gene regulation in bacteria: making progress towards a unified model? *Nat. Rev. Microbiol.* **11** 349–55
- [12] Lampo T J, Kuwada N J, Wiggins P A and Spakowitz A J 2015 Physical modeling of chromosome segregation in *Escherichia coli* reveals impact of force and dna relaxation *Biophys. J.* **108** 146–53
- [13] Paul B, Ross W, Gaal T and Gourse R 2004 rRNA transcription in *Escherichia coli* *Annu. Rev. Genet.* **38** 749–70
- [14] Dame R T, Kalmykova O J and Grainger D C 2011 Chromosomal macrodomains and associated proteins: implications for DNA organization and replication in gram negative bacteria *PLoS Genet.* **7**
- [15] Espeli O, Mercier R and Boccard F 2008 DNA dynamics vary according to macrodomain topography in the *Mol. Microbiol.* **68** 1418–27
- [16] Weber S C, Spakowitz A J and Theriot J A 2010 Bacterial chromosomal loci move subdiffusively through a viscoelastic cytoplasm *Phys. Rev. Lett.* **104** 27–30
- [17] Javer A, Long Z, Nugent E, Grisi M, Siriawetchakul K, Dorfman K D, Cicuta P and Cosentino Lagomarsino M 2013 Short-time movement of *E. coli* chromosomal loci depends on coordinate and subcellular localization *Nat. Commun.* **4** 3003
- [18] Cass J A, Kuwada N J, Traxler B and Wiggins P A 2016 *Escherichia coli* chromosomal loci segregate from midcell with universal dynamics *Biophys. J.* **110** 2597–609
- [19] Waigh T A 2005 Microrheology of complex *Rep. Prog. Phys.* **68** 685–742
- [20] Cicuta P and Donald A M 2007 Microrheology: a review of the method and applications *Soft Matter* **3** 1449
- [21] Bouchaud J P and Georges A 1990 Anomalous diffusion in disordered media: statistical mechanisms, models and physical applications *Phys. Rep.* **195** 127–293
- [22] MacKintosh F C 2012 Active diffusion: The erratic dance of chromosomal loci *Proc. Natl. Acad. Sci.* **109** 7138–9
- [23] Espeli O and Boccard F 2006 Organization of the *Escherichia coli* chromosome into macrodomains and its possible functional implications *J. Struct. Biol.* **156** 304–10
- [24] Weber S C, Spakowitz A J and Theriot J A 2012 Nonthermal ATP-dependent fluctuations contribute to the in vivo motion of chromosomal loci *Proc. Natl. Acad. Sci. USA* **109** 7338–43
- [25] Javer A, Kuwada N J, Long Z, Benza V G, Dorfman K D, Wiggins P A, Cicuta P and Lagomarsino M C 2014 Persistent super-diffusive motion of *Escherichia coli* chromosomal loci *Nat. Commun.* **5** 3854
- [26] Espeli O, Borne R, Dupaigne P, Thiel A, Gigant E, Mercier R and Boccard F 2012 A MatP-divisome interaction coordinates chromosome segregation with cell division in *E. coli* *EMBO J.* **31** 3198–211
- [27] Sobetzko P, Travers A and Muskhelishvili G 2012 Gene order and chromosome dynamics coordinate spatiotemporal gene expression during the bacterial growth cycle *Proc. Natl. Acad. Sci. USA* **109** E42–50
- [28] Parry B R, Surovtsev I V, Cabeen M T, O’Hern C S, Dufresne E R and Jacobs-Wagner C 2014 The bacterial cytoplasm has glass-like properties and is metabolic activity *Cell* **156** 183–94
- [29] Bernstein J A, Lin P H, Cohen S N and Lin-Chao S 2004 Global analysis of *Escherichia coli* RNA degradosome function using DNA microarrays *Proc. Natl. Acad. Sci.* **101** 2758–63
- [30] Cabrera J E and Jin D J 2006 Active transcription of rRNA operons is a driving force for the distribution of RNA polymerase in bacteria: effect of extrachromosomal copies of *rrnB* on the in vivo localization of RNA polymerase *J. Struct. Biol.* **188** 4007–14
- [31] Bakshi S, Choi H, Mondal J and Weisshaar J C 2014 Time-dependent effects of transcription- and translation-halting drugs on the spatial distributions of the *E. coli* chromosome and ribosomes *Mol. Microbiol.* **94** 871–87
- [32] Romero D, Traxler M F, López D and Kolter R 2011 Antibiotics as signal molecules *Chem. Rev.* **111** 5492–505
- [33] Khil P P and Camerini-Otero R D 2002 Over 1000 genes are involved in the DNA damage response of *Escherichia coli* *Mol. Microbiol.* **44** 89–105
- [34] Shaw K J, Miller N, Liu X, Lerner D, Wam J, Bittner A and Morrow B 2003 Comparison of the changes in global gene expression of *Escherichia coli* induced by four bactericidal agents *J. Mol. Microbiol. Biotechnol.* **5** 105
- [35] Long Z, Nugent E, Javer A, Cicuta P, Sclavi B, Cosentino Lagomarsino M and Dorfman K D 2013 Microfluidic chemostat for measuring single cell dynamics in bacteria *Lab Chip* **13** 947–54
- [36] Wang P, Robert L, Pelletier J, Dang W L, Taddei F, Wright A and Jun S 2010 Robust growth of *Escherichia coli* *Curr. Biol.* **20** 1099–103
- [37] Kaiser M, Jug F, Silander O, Deshpande S, Julou T, Myers G and Nimwegen E V 2016 Tracking single-cell gene regulation in dynamically controlled environments using an integrated micro bioRxiv (doi: [10.1101/076224](https://doi.org/10.1101/076224))
- [38] Rocha E P C 2008 The organization of the bacterial genome *Annu. Rev. Genet.* **42** 211–33
- [39] Broering T J, Parker J S L, Joyce P L, Kim J and Nibert M L 2002 Mammalian reovirus nonstructural protein NS forms large inclusions and colocalizes with reovirus microtubule-associated protein 2 in transfected cells *J. Virol.* **76** 8285–97
- [40] Broering T J, Arnold M M, Miller C L, Hurt J A, Joyce P L and Nibert M L 2005 Carboxyl-proximal regions of reovirus nonstructural protein NS necessary and sufficient for forming factory-like inclusions *J. Virol.* **79** 6194–206
- [41] Wiegand I, Hilpert K and Hancock R E W 2008 Agar and broth dilution methods to determine the minimal inhibitory concentration (MIC) of antimicrobial substances *Nat. Protoc.* **3** 163–75